



Article

A Priori Knowledge Based Ground Moving Target Indication Technique Applied to Distributed Spaceborne SAR System

Bin Cai ^{1,*}, Xiaolong Hao ², Li Chen ², Jia Liang ¹, Tianhao Cheng ¹ and Ying Luo ¹

¹ The Institute of Information and Navigation, Air Force Engineering University, Xi'an 710077, China

² Beijing Institute of Tracking and Telecommunication Technology, Beijing 100089, China

* Correspondence: caibin2004@aliyun.com

Abstract: Through formation flying, the distributed spaceborne SAR (synthetic aperture radar) system can increase the number of spatial degree of freedoms (DOFs) and provide flexible multi-baselines for SAR-GMTI (ground moving target indication), which improves the system performance. This paper proposes an a priori knowledge-based adaptive clutter cancellation and moving target detection technique applied to the distributed spaceborne SAR-GMTI systems. Firstly, the adaptive clutter cancellation technique is exploited to suppress the ground clutter. A priori knowledge, such as road network information, is integrated to the adaptive clutter cancellation processor to reduce any moving target steering vector mismatch. Secondly, adaptive matched filter (AMF) and adaptive beamformer orthogonal rejection test (ABORT) are exploited as adaptive detection techniques for moving target detection. Due to the dense road network, the moving target steering vector estimation may be ambiguous for the different position and orientation of the roads. The multiple hypothesis testing (MHT) technique is proposed to detect the moving targets and resolve the potential ambiguities. A scheme is exploited to detect, classify, and relocate the moving targets. Finally, simulation experiments and performance analysis have demonstrated the effectiveness and robustness of the proposed technique.

Keywords: distributed spaceborne SAR; GMTI; a priori knowledge; adaptive clutter cancellation; adaptive detection technique; multiple hypothesis testing



Citation: Cai, B.; Hao, X.; Chen, L.; Liang, J.; Cheng, T.; Luo, Y. A Priori Knowledge Based Ground Moving Target Indication Technique Applied to Distributed Spaceborne SAR System. *Remote Sens.* **2023**, *15*, 2467. <https://doi.org/10.3390/rs15092467>

Academic Editor: Andrzej Stateczny

Received: 4 January 2023

Revised: 25 April 2023

Accepted: 1 May 2023

Published: 8 May 2023



Copyright: © 2023 by the authors. Licensee MDPI, Basel, Switzerland. This article is an open access article distributed under the terms and conditions of the Creative Commons Attribution (CC BY) license (<https://creativecommons.org/licenses/by/4.0/>).

1. Introduction

Spaceborne SAR-GMTI systems combine high-resolution SAR (synthetic aperture radar) imaging with the GMTI (ground moving target indication) technique to observe the stationary scene and detect moving targets on the ground. In addition to the large coverage of the spaceborne SAR sensor, its day-and-night and all-weather capabilities make it a very interesting tool for traffic management, detection of ground slowly moving targets for military use, and other uses. The planned single-pass distributed spaceborne SAR [1] can provide large and flexible along-track baselines to enhance clutter cancellation performance and decrease the minimum detectable velocity (MDV) for GMTI. However, due to high satellite velocity and the long range between satellites and the earth, suppression of clutter and detection of ground slowly moving targets become a difficult task for spaceborne SAR.

The distributed spaceborne SAR-GMTI systems, multibaseline/multichannel ATI (along track interferometry)/DPCA (displaced phase center antenna), and adaptive clutter suppression techniques applied to the SAR image or Doppler domain are always exploited as clutter cancellation techniques [2–5]. Based on the short/long multiple baselines, the high-resolution SAR satellites TerraSAR-X (TSX) and TanDEM-X (TDX) utilized the bistatic SAR-ATI technique to get highly accurate velocity estimates for slow and fast target movement [6,7]. In [8,9], the joint pixel eigendecomposition method is proposed to resolve the SAR image misregistration in the linear clutter suppression scheme for distributed spaceborne SAR-GMTI. In [10], based on the multi-channel SAR images, a radial velocity

estimation algorithm is proposed to mitigate the effect of heterogeneous clutter using the joint-pixel normalized sample covariance matrix and the shift vector. F.Meyer and S.Hinz et al. [11–14] integrated a priori information into the SAR-ATI technique for traffic monitoring with TSX. In reality, except for some special military applications of GMTI, a large majority of targets may travel strictly on roads or highways in a specific direction and within a velocity range. The integration of a priori information into SAR-GMTI was suited for theoretical and engineering applications. In [15], the optimum linear clutter filter integrated with a priori information applied to spaceborne dual-channel SAR-GMTI is proposed, which maximizes the output signal-to-clutter plus noise ratio(SCNR). S.V. Baumgartner et al. [16–18] proposed an a priori knowledge-based ground moving target indication and parameter estimation algorithm applicable to single as well as to multichannel synthetic aperture airborne radars. In [19], for a multichannel SAR-GMTI system, the along-track baseline is derived based on the subspace projection, where the target radial velocity is estimated according to the azimuth position offset by exploiting the road-aided information. A.Budillon et al. [20] determined that it is difficult to use the road map as a priori information for the dense road network, but the prior road information can be used to assess the GMTI performance. C.Song et al. [21] proposed a GLRT detection method to detect the moving targets for multichannel SAR. In [22,23], a robust optimum adaptive clutter suppression technique for SAR-GMTI applied to the distributed spaceborne SAR, which includes the diagonal loading technique with a priori information integrated into the processor. Research in the area of moving targets detection in the presence of clutter has resulted in a number of adaptive detection algorithms. In general, the generalized likelihood ratio test (GLRT) is always exploited for moving target detection for multistatic or multi-channel SAR-GMTI techniques [15,21–23]. Traditional detectors can suppress clutter and achieve detection. In reality, AMF and ABORT are the two well-known adaptive techniques for radar target detection. The AMF exhibits robust behavior with respect to steering vector mismatches and more computational efficiency than many other detectors as the generalized likelihood ratio test (GLRT) [15,21–23]. The ABORT can reject interference signals orthogonal to the nominal steering direction, which modifies the null hypothesis to the unwanted signal assumed to be orthogonal to the nominal steering vector.

In this paper, a priori knowledge-based adaptive clutter cancellation and moving target detection techniques for SAR-GMTI are applied to the distributed spaceborne SAR systems. The technique is applied to the formation flying that the distributed satellites exhibit as they fly along the same orbit arc as seen from the ground. The phase centers of these satellites are aligned to form a sparse linear array [1]. A priori knowledge, such as the roads information predicted from the road network database, is integrated into the adaptive processor to reduce moving target steering vector mismatch. Two traditional adaptive detection techniques, which include the adaptive matched filter (AMF) and the adaptive beamformer orthogonal rejection test (ABORT), are exploited to detect moving targets in clutter. If the road network is so dense that the azimuth displacement and the moving target steering vector estimation may be ambiguous for different positions and orientations of the roads [11–14], the multiple hypothesis testing technique (MHT) is proposed to detect the targets and resolve the potential ambiguities. The detection, classification and relocation scheme are exploited to detect the presence of a target, correctly classify, and relocate it to the corresponding roads. Performance is investigated by means of Monte Carlo simulations in terms of probability of false alarm, detection, and classification. To verify the distributed spaceborne SAR processing scheme and simplify the instrument hardware design, our research group designed the commercial simulation software named SpaceBorne Radar Advanced Simulator (SBRAS) [24,25]. Simulation results developed on SBRAS and performance analysis demonstrate the effectiveness and robustness of the proposed method.

The paper is organized as follows: Section 2 reviews the signal model under Gaussian assumption of clutter and states the adaptive clutter cancellation technique. Section 3 analyzes the moving target steering vector mismatch and integrates a priori knowledge

to the adaptive clutter cancellation processor. Section 4 analyzes two traditional adaptive detection techniques and proposes the MHT technique. Performance has been investigated either analytically or by means of Monte Carlo simulation in terms of probabilities of false alarm, detection, and correct classification. Section 5 gives the simulation experimental results and analysis based on SBRAS. Section 6 gives the conclusions.

This paper is an extension of our conference papers presented at the IET International Radar Conference in 2009 [15] and at the International Conference on Computer Application and System Modeling in 2010 [22]. This paper is an extension of the first author's PhD thesis [23].

2. Signal Model and Adaptive Clutter Cancellation

Consider K identical spaceborne SARs flying along the same orbit when viewed from the ground. This semiactive configuration is named SAR-Train [1]. The K SAR flies on the same orbital arc in an Earth frame, which means that the SARs are generally on different orbit planes because of the across orbit Earth rotation between successive passes. The main formation flying constraint is the width of the tube containing the satellite trajectories. The time intervals between the satellites, which cause the temporal decorrelation of the backscatter, is supposed to be very short. In the train of K monostatic/bistatic spaceborne SARs, the first satellite known as master satellite transmits/receives radar signal/echo, while other satellites, known as slave satellites, only receive the radar echo. The phase centers of these satellite constellations are aligned to form a sparse linear array. Based on the configurations and the monostatic/bistatic SAR imaging techniques, the K phase centers focus on the processed point at different times [6,15,22,23]. The complex SAR images of the same area can be obtained with identical geometry of every satellite and with uniform/nonuniform along-track baselines. In other words, the multi-aperture SAR images are sampled with time delay determined by baseline permutation and combination. Image alignment can be performed in the coregistration stage.

Firstly, some realistic assumptions are described as follows: (1) since the along-track baseline distance is short for the multibaseline spaceborne SAR-GMTI system, the target's movement is smaller than the resolution cell size within the small time delay; (2) stationary clutter is modeled as a Gaussian distributed process; (3) the multilook SAR resolution cell size is larger than the spatial dimension of the target that contains both clutter and the moving target; the clutter power can no longer be neglected; (4) moving target travel with constant velocity without acceleration or brake; (5) magnitude and phase errors caused by mismatched SAR processing or channel unbalance have been eliminated prior to the detection [26]; and (6) the subpixel coregistration precision can be obtained using the maximum-spectrum image registration method.

Two hypotheses H_0 and H_1 are defined as clutter and noise (H_0) and signal plus clutter and noise (H_1). For image pixel index (m, n) , the K dimensional SAR image vector can be modeled as the following [15,22,23],

$$\begin{aligned} \text{Hypothesis } H_0 : \vec{Z}(m, n) &= \vec{C}(m, n) + \vec{N}(m, n) \\ \text{Hypothesis } H_1 : \vec{Z}(m, n) &= \vec{S}(m, n) + \vec{C}(m, n) + \vec{N}(m, n) \end{aligned} \quad (1)$$

where \vec{C} is the clutter vector that is assumed to be independent with an identically distributed (i.i.d.) circular Gaussian with zero mean in the local terrain. \vec{N} is the additive noise vector. The moving target's signal vector \vec{S} is modeled as a statistically independent point target. $\vec{S}(m, n) = \beta \vec{a}(\psi) \odot \vec{S}_{Nor}(m, n)$. $\vec{S}_{Nor}(m, n)$ is the normalized complex moving target's image pixel vector. β is the amplitude of the moving target. $\vec{a}(\psi)$ is the normalized

spatial steering vector. γ is the unknown moving target’s interferometric phase between the master and the first slave satellite. \odot is the Shur–Hadamard product. Furthermore,

$$\vec{a}(\psi) = \frac{1}{\sqrt{K}} [1, \exp(-j\psi), \exp(-j\psi \frac{B_{1,3}}{B_{1,2}}), \dots, \exp(-j\psi \frac{B_{1,K-1}}{B_{1,2}}), \exp(-j\psi \frac{B_{1,K}}{B_{1,2}})]^T \tag{2}$$

where $(\bullet)^T$ denotes the transpose operator. $B_{1,i} (i = 2, \dots, K)$ are the along-track baselines between the master and the i th slave satellite. K is the number of spaceborne SARs with transmitters and receivers. The adaptive clutter cancellation processor can be expressed as,

$$\vec{y}(m, n) = \vec{W}(m, n)^H \cdot \vec{Z}(m, n) \tag{3}$$

where \vec{y} is the output, \vec{W} is the weight of the processor, and $(\bullet)^H$ denotes the Hermitian transpose. Under some well-known optimal criteria, the processor can be given in a more general form as,

$$\vec{W}(m, n) = \gamma R^{-1}(m, n) \cdot \vec{S}(m, n) \tag{4}$$

where R denotes the clutter plus noise covariance matrix. The complex constant γ is selected according to the following criteria. Under linearly constrained minimum expectation power criterion, the normalization constant $\gamma = 1 / \sqrt{\vec{S}(m, n)^H R^{-1}(m, n) \vec{S}(m, n)}$. γ can be arbitrarily chosen for the maximum SCNR criterion.

Similar to traditional adaptive beamforming or adaptive clutter cancellation techniques for GMTI, R is unknown and is usually estimated using the maximum likelihood (ML) technique. Assume that the neighboring $2K_m * 2K_n$ samples around pixel (m, n) are available, which are free from any moving target signals and identically distributed. Then the sample clutter plus noise matrix of pixel index (m, n) is [15,22,23],

$$\hat{R}(m, n) = \frac{1}{2K_m * 2K_n} \sum_{k_m=-K_m, k_m \neq 0}^{k_m=K_m} \sum_{k_n=-K_n, k_n \neq 0}^{k_n=K_n} \left(\vec{Z}(m - k_m, n - k_n) \cdot \vec{Z}(m - k_m, n - k_n)^H \right) \tag{5}$$

In practice, $\vec{a}(\psi)$ is always unknown and the scanning method is always exploited to get the estimation $\hat{\vec{a}}(\psi)$ for the matched filter, which is a computationally intensive technique. The Equation (4) can be computed as,

$$\hat{W}(m, n) = \gamma \hat{R}^{-1}(m, n) \cdot \hat{S}(m, n) \tag{6}$$

The adaptive clutter cancellation processor can be expressed as,

$$\hat{\vec{y}}(m, n) = \hat{W}(m, n)^H \cdot \vec{Z}(m, n) \tag{7}$$

3. Problem Statements and A Priori Knowledge Integration

3.1. Moving Target Steering Vector Mismatch

As shown in Equation (6), the adaptive clutter cancellation processor is to estimate the moving target steering vector $\vec{a}(\psi)$ using the scanning method in the presence of clutter and noise. The goal, of course, is to search the desired steering vector quickly with a high degree of reliability. In reality, the estimation might be obscured by high clutter, noise, and a distorted beampattern, which is always called moving target steering vector mismatch.

The total available output SCNR for the adaptive clutter cancellation can be denoted as [15,22],

$$SCNR_{outtotal} = \beta^2 \cdot \vec{a}(\psi)^H R^{-1} \vec{a}(\psi) \tag{8}$$

After SAR processing, the definition of *SCNR* is somewhat different from the usual definition in STAP (space time adaptive processing) [27]. The *SCNR* can be defined as,

$$SCNR = \frac{(N_r N_a) \frac{P_T G_T G_R \lambda^2 \sigma_s}{(4\pi)^3 r_t^4}}{(N_r N_a) \frac{P_T G_T G_R \lambda^2 \sigma_c^0 \rho_a \rho_r}{(4\pi)^3 r_t^4} + K_B T B} \quad (9)$$

where σ_s is the radar cross-section (RCS) of the moving targets. σ_c^0 is the mean RCS of the stationary terrain. ρ_a and ρ_r are the SAR azimuth and range resolution. r_t is the target's slant range distance. λ is the radar wavelength. P_T is the radar transmitting power. K_B is the Boltzmann constant. G_T, G_R are the radar transmitter and receiver antennas gain. T is the radar receiver noise temperature. B and T are the radar receiver bandwidth temperature. N_r, N_a are the SAR processing of range samples and azimuth samples.

In practice, the detectable output *SCNR* is sensitive to mismatches between the searched and actual target steering vectors. We define θ as the mismatch angle between the searched and actual target steering vector $\hat{\vec{a}}, \vec{a}$ [15,22,23,28–30].

$$\cos^2(\theta) = \frac{\left| \hat{\vec{a}}(\psi)^H R^{-1} \vec{a}(\psi) \right|^2}{\left(\hat{\vec{a}}(\psi)^H R^{-1} \hat{\vec{a}}(\psi) \right) \left(\vec{a}(\psi)^H R^{-1} \vec{a}(\psi) \right)} \quad (10)$$

The available output *SCNR* for target steering vector mismatch can be shown as [15,22,28–30],

$$SCNR_{out} = \beta^2 \cdot \vec{a}(\psi)^H R^{-1} \vec{a}(\psi) \cdot \cos^2(\theta) \quad 0 \leq \cos^2 \theta \leq 1 \quad (11)$$

Note that $\cos^2(\theta)$ partially captures the effect of steering vector mismatch, where $\hat{\vec{a}}$ and \vec{a} point in different directions. $\cos^2(\theta) = 0$ represents that the estimated steering vectors are orthogonal to the real steering vectors. Similarly, $\cos^2(\theta) = 1$ represents that the estimated steering vectors are matched to the real steering vectors. If the filter is steered in the wrong direction, only a fraction of the total output *SCNR* is usable. The adaptive search of the target steering vector is a time-consuming process, and the resolution is limited by the sample number, number of satellites, and the baselines' length. Except for some traditional causes, the presence of partially correlated speckle and additive noise has the effect of increasing the variance of the target steering vector.

3.2. Integration of A Priori Knowledge

Except for some military applications of GMTI, a great deal of targets may travel strictly on the road with a specific moving direction and velocity range. These types of prediction may be interpreted as a priori knowledge that can be acquired, analyzed, and stored independent of image acquisition. In this paper, road network databases serve as a basic source for acquiring a priori knowledge. These databases contain road axes in the form of polygons and attributes, such as road width, maximum velocity, and road direction. S.V. Baumgartner et al. [16–18] proposed a method to transform the geographical coordinates of each road point to corresponding azimuth beam center coordinates in the airborne radar range/azimuth plane. The azimuth beam center position of the detected moving vehicle is then directly given by the intersection of the vehicle signal with the mapped road point. The road network stored in the databases may represent all possible moving target positions in a real scene. In this paper, based on the road network database and SAR images, the displacement map and moving target interferometric phase map around the roads can be computed pixel by pixel [11–14,22,23].

In the single SAR transmits and several SAR receive modes, the moving target interferometric phase ψ can be expressed as [11–14,22,23],

$$\psi = \frac{2\pi v_r B_{1,2}}{\lambda v_s} \quad (12)$$

where v_r is the target ground radial velocity and v_s is the satellite velocity. The azimuth displacement Δa is defined as [11–14,22,23],

$$\Delta a = a_t - a_{road} \quad (13)$$

where a_t is the moving target azimuth position in the SAR image and a_{road} is the corresponding road segment position. The azimuth displacement is also caused by the target's across-track motion, which occurred due to SAR focusing. Δa is always exploited to compute the targets' interferometric phase and across-track velocities [11–14,22,23].

$$\Delta a = \frac{2v_r v_g}{\lambda f_r} = \frac{\psi v_g v_s}{\pi f_r B_{1,2}} \quad (14)$$

where f_r is the Doppler frequency modulation rate and v_g is the radar beam velocity on the ground.

For the master satellite SAR, which both transmits and receives the radar signal, f_r can be computed as,

$$f_r = -2v_g^2 / \lambda r_t \quad (15)$$

$$\Delta a = -\frac{v_r r_t}{v_g} = -\frac{r_t \psi \lambda}{4\pi B_{1,2}} \quad (16)$$

Firstly, based on the road network database and radar parameters, the displacement measurements of every pixel around its corresponding road segments in the SAR images, which is called as displacement map, can be computed according to Equation (13). Secondly, the moving target's interferometric phase map can be computed directly using the displacement map according to Equation (14). Finally, the moving target steering vectors estimation can be computed using Equation (2). In Equation (6), the searched moving target steering vectors can be directly replaced by estimation results from the interferometric phase map, which can reduce the steering vector mismatch effectively. The expected moving target steering vectors, which are derived from the interferometric phase map, can be directly integrated to the adaptive clutter cancellation processor. The estimation accuracy has been analyzed in the paper [11–14,22]. In Section 4, the expected steering vectors can also be directly integrated into the two kinds of adaptive detection techniques, in which the searched steering vectors are also replaced by the estimation results derived from the interferometric phase map.

Compared with the traditional adaptive clutter cancellation technique according to Equations (1)–(4), the proposed a priori knowledge-based adaptive clutter cancellation technique replaced the moving target steering vector searched results with the estimated results. The estimated results of the moving target steering vector are based on the road network database, the SAR images, the displacement map, and the moving targets interferometric phase map. According to Equations (12)–(16), the displacement map and the moving targets interferometric phase map are computed based on the road information, the SAR images, and the radar or satellite parameters. On one hand, the road information can be computed according to the road network database. On the other hand, the road recognition results of the SAR images and the road information can be combined to determine the road location in the SAR images.

In reality, the road network is so dense that the Δa and ψ estimation may overlap for different roads. A target detected in such an area has several possible Δa and ψ estimates. The moving target steering vector estimation may be ambiguous for different positions and

orientations of the roads [11–14]. The multiple hypothesis testing technique is proposed to resolve the potential ambiguities and detect the moving targets.

4. Multiple Hypothesis Testing Technique

4.1. Adaptive Detection Techniques

Research in the area of moving targets detection in the presence of clutter has resulted in a number of adaptive detection algorithms. AMF [31,32] and ABORT [29,30] are the two well-known techniques. The AMF exhibits robust behavior with respect to steering vector mismatches and more computational efficiency than many other detectors as the generalized likelihood ratio test (GLRT) and adaptive coherence estimator (ACE) [15,22,23]. The ABORT can reject interference signals orthogonal to the nominal steering direction, which modifies the null hypothesis to the unwanted signal assumed to be orthogonal to the nominal steering vector [29,30]. Traditional AMF can be expressed in the formula as [28–32],

$$\Lambda_{AMF} = \frac{\left| \frac{\hat{S}^H}{\hat{S}} \hat{R}^{-1} \vec{Z} \right|^2}{\frac{\hat{S}^H}{\hat{S}} \hat{R}^{-1} \frac{\hat{S}}{\hat{S}}} = \frac{\left| \frac{\hat{W}^H}{\hat{W}} \vec{Z} \right|^2}{\frac{\hat{W}^H}{\hat{W}} \hat{R} \frac{\hat{W}}{\hat{W}}} \underset{H_0}{\overset{H_1}{\geq}} \eta_{AMF} \tag{17}$$

where $\left| \frac{\hat{W}^H}{\hat{W}} \hat{R}^{-1} \vec{W} \right|^2$ is often known as the normalization coefficient. η_{AMF} is the threshold which is chosen according to the desired false alarm probability. As shown in [30], we choose to replace \hat{R} , Λ_{AMF} with \hat{R}' , Λ'_{AMF} for performance analysis ease.

$$\hat{R}'(m, n) = \sum_{k_m=-K_m, k_m \neq 0}^{k_m=K_m} \sum_{k_n=-K_n, k_n \neq 0}^{k_n=K_n} \left(\vec{Z}(m - k_m, n - k_n) \cdot \vec{Z}(m - k_m, n - k_n)^H \right) = K_{mn} \hat{R}(m, n) \tag{18}$$

$$\Lambda'_{AMF} = \frac{\left| \frac{\hat{S}^H}{\hat{S}} \hat{R}'^{-1} \vec{Z} \right|^2}{\frac{\hat{S}^H}{\hat{S}} \hat{R}'^{-1} \frac{\hat{S}}{\hat{S}}} \underset{H_0}{\overset{H_1}{\geq}} \eta'_{AMF} \tag{19}$$

where $K_{mn} = 2K_m * 2K_n$, which is the number of the neighboring samples to estimate R, R' . $\eta_{AMF} = K_{mn} \eta'_{AMF}$, $\Lambda_{AMF} = K_{mn} \Lambda'_{AMF}$. $\hat{R}'(m, n)$ is replaced by \hat{R}' for ease of expression.

The test statistic of the ABORT is [30],

$$\Lambda_{ABORT} = \frac{1 + \frac{\left| \frac{\hat{S}^H}{\hat{S}} \hat{R}'^{-1} \vec{Z} \right|^2}{\frac{\hat{S}^H}{\hat{S}} \hat{R}'^{-1} \frac{\hat{S}}{\hat{S}}}}{1 + \frac{\hat{S}^H}{\hat{S}} \hat{R}'^{-1} \vec{Z} - \frac{\left| \frac{\hat{S}^H}{\hat{S}} \hat{R}'^{-1} \vec{Z} \right|^2}{\frac{\hat{S}^H}{\hat{S}} \hat{R}'^{-1} \frac{\hat{S}}{\hat{S}}}} = \tau + \frac{\left| \frac{\hat{S}^H}{\hat{S}} \hat{R}'^{-1} \vec{Z} \right|^2}{\frac{\hat{S}^H}{\hat{S}} \hat{R}'^{-1} \frac{\hat{S}}{\hat{S}}} \underset{H_0}{\overset{H_1}{\geq}} \tau \bullet \eta_{ABORT} \tag{20}$$

$$\Lambda_{ABORT} = \frac{1 + \Lambda'_{AMF}}{1 + \frac{\hat{S}^H}{\hat{S}} \hat{R}'^{-1} \vec{Z} - \Lambda'_{AMF}} = \tau + \Lambda'_{AMF} \bullet \underset{H_0}{\overset{H_1}{\geq}} \eta_{ABORT}$$

Define the loss factor τ as [30],

$$\tau = \frac{1}{1 + \frac{\hat{S}^H}{\hat{S}} \hat{R}'^{-1} \vec{Z} - \Lambda'_{AMF}}, 0 \leq \tau \leq 1 \tag{21}$$

The P_d (probability of detection) and P_{fa} (probability of false alarm) are given as [23,30],

$$P_{d(\bullet)} = \int_0^1 P_{d(\bullet)|\tau} \cdot P_{\tau} d\tau, P_{fa(\bullet)} = \int_0^1 P_{fa(\bullet)|\tau} \cdot P_{\tau} d\tau \tag{22}$$

where (\bullet) denotes AMF and ABORT. As shown in Equations (19) and (20), when the moving target steering vector mismatch existed as $\theta \neq 0$, τ follows the complex non-central

beta distribution [23,29,30]. When the moving target steering vector mismatch did not exit, τ follows the complex central beta distribution. The conditional $P_{fa} P_{fa(\bullet)|\tau}$ and $P_d P_{d(\bullet)|\tau}$ can also be expressed as,

$$P_{fa(\bullet)|\tau} = \int_0^{\tilde{\eta}(\bullet)} \Pr(\Lambda_{(\bullet)}|\tau) d\Lambda_{(\bullet)}, P_{d(\bullet)|\tau} = \int_{\tilde{\eta}(\bullet)}^{+\infty} \Pr(\Lambda_{(\bullet)}|\tau) d\Lambda_{(\bullet)} \tag{23}$$

The alternative threshold $\tilde{\eta}(\bullet)$ for AMF and ABORT are defined as,

$$\tilde{\eta}_{AMF} = \tau \eta'_{AMF}, \tilde{\eta}_{ABORT} = \eta_{ABORT} - \tau \tag{24}$$

As shown in [23,29,30], the $P_{fa(\bullet)|\tau}$ can also be expressed in the simple formulation,

$$P_{fa(\bullet)|\tau} = 1 / (1 + \tilde{\eta}(\bullet))^L \tag{25}$$

$P_{d(\bullet)|\tau}$ is [23,29,30],

$$P_{d(\bullet)|\tau} = 1 - \frac{1}{(1 + \tilde{\eta}(\bullet))^L} \sum_{l=1}^L \binom{L}{l} \cdot \tilde{\eta}^l(\bullet) G_l \left(\frac{SCNR_{out}\tau}{1 + \tilde{\eta}(\bullet)} \right) \tag{26}$$

where $G_l(*)$ is the incomplete Gamma function $L = K_{mn} - K + 1$. According to the Equations (19)–(26), we can analyze the detection performance loss for AMF and ABORT under different mismatch angles θ .

Figure 1 is a plot of the Pd versus $\cos^2(\theta)$ of the above two detection algorithms with parameters $L = 49, K = 6, P_{fa} = 10^{-5}, SCNR_{out} = 20dB$. As shown in Figure 1, with the increase of the mismatch angle θ , the Pd of the two detection algorithms decrease quickly. AMF is much more robust for target steering vector mismatches and has similar detection performance to ABORT for the large $\cos^2(\theta)$ case. For ABORT, if the mismatch angle θ is so large, then the Pd may approximate to zero. Figure 2 shows the ROC (Receiver Operating Characteristic) curves, which are Pd versus Pfa in log scale with parameters $L = 49, K = 6, SCNR_{out} = 10dB, \theta = 0, pi/5$. Figure 2 shows that AMF and ABORT have approximate detection performance for the $\theta = 0$ case, especially under low Pfa. For the $\theta = pi/5$ case, AMF has a much better detection performance than the ABORT. With the increase of mismatch angle θ , the performance of the ROC for the two detection algorithms decrease very obviously.

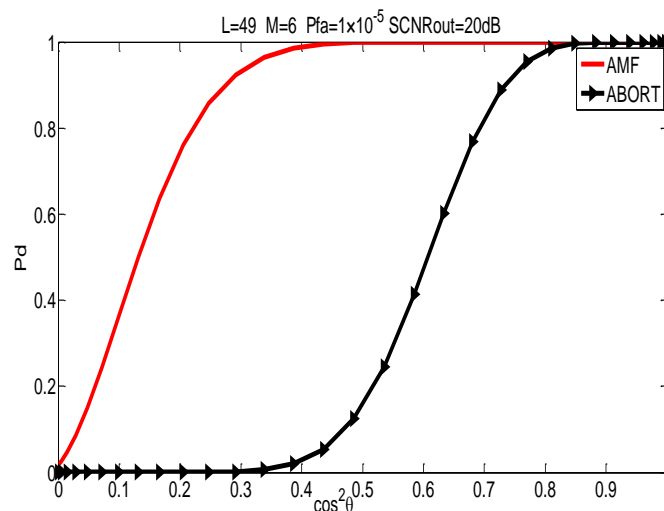


Figure 1. Pd versus $\cos^2(\theta)$ for AMF and ABORT.

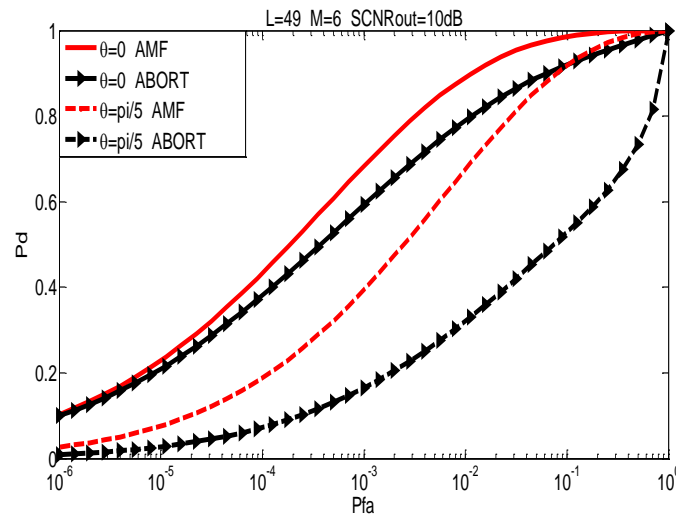


Figure 2. ROC(Pd versus Pfa in log scale) for AMF and ABORT.

As shown in Figures 1 and 2, when the steering vector mismatch increases, the detection performance for the two adaptive detection techniques decreases largely. AMF has much better mismatch discrimination capabilities than ABORT. In this paper, based on the a priori knowledge of the road network database, the expected steering vectors are derived directly from the interferometric phase map and azimuth displacement map. In Equations (19) and (20), the searched moving target steering vectors are replaced by steering vector estimation results from the interferometric phase map and displacement map.

4.2. Multiple Hypothesis Testing Technique

For most motorways and less dense road networks, the moving targets' interferometric phases can easily be determined using their azimuth displacement. For dense road networks, the roads are so close that the azimuth displacement intervals overlap. A moving target in such an area may have several possible azimuth displacement and interferometric phase estimates because the Δa and $\vec{a}(\psi)$ estimations are linked by the position and orientation of the roads. The wrong road assignments and steering vector estimates may lead to false detections, velocity estimation ambiguities, and false relocations. Since the moving target steering vector estimation is linked to the position and orientation of the roads, they can be exploited as a likelihood ratios test (LRT) function indicating the probability of moving target detection and the true corresponding road that the detected targets belong to. The multiple hypothesis testing technique [23,33,34] is proposed in this paper to robustly resolve potential ambiguities in the moving target phase estimation.

Define the $M + 1$ hypotheses as H_0 and $H_k, k=1, \dots, M$. H_0 : clutter plus noise. H_k : the k th signal plus clutter and noise, and the target belongs to the k th road. Therefore, the signal model in Equation (1) can be modified as,

$$\begin{aligned} \text{Hypothesis } H_0 : \vec{Z}(m, n) &= \vec{C}(m, n) + \vec{N}(m, n) \\ \text{Hypothesis } H_k : \vec{Z}(m, n) &= \vec{S}_k(m, n) + \vec{C}(m, n) + \vec{N}(m, n), \quad k = 1 \dots M \end{aligned} \quad (27)$$

In Equation (27), $\vec{S}_k(m, n) = \beta \vec{a}_k(\psi) \odot \vec{S}_{Nor}(m, n)$. $\vec{a}_k(\psi)$ is the moving target's spatial steering vector and the target belongs to the k th road. $\vec{a}_k(\psi)$ can be estimated from road network database and radar parameters using Equations (12)–(14). A priori probability of hypothesis H_k is denoted by $P(H_k) = \text{Probability}\{H_k\}$, $k = 1 \dots M$. We assume that $P(H_k)$, $k = 1 \dots M$ are unknown, but those pertaining to the target classes are all the same. As such, $P_k = (1 - P_0)/M$, $k = 1 \dots M$, where P_0 is the probability of the hypothesis H_0 .

In this paper, we propose a detection, classification, and relocation scheme, which can detect the presence of a target and correctly classify it to corresponding roads. Based on road network database and SAR image, the detected and classified targets can be relocated to corresponding locations on the road. We propose to exploit the multiple hypothesis testing strategy, which needs to calculate all the likelihood ratios between each pair of hypotheses and compare each likelihood ratio with a proper threshold. For the MHT strategy, to compute the H_0 versus H_j and H_j versus $H_{j'}$, we may exploit the AMF technique as Equation (19) and the ABORT technique as Equation (20).

$$\Lambda_{0,k(AMF)} = \frac{\left| \frac{\hat{\Delta}^H}{S_k} \hat{R}'^{-1} \hat{\Delta} \right|^2}{\frac{\hat{\Delta}^H}{S_k} \hat{R}'^{-1} \hat{\Delta}} = \frac{\left| \frac{\hat{\Delta}^H}{W} \hat{\Delta} \right|^2}{\frac{\hat{\Delta}^H}{W} \hat{\Delta}} \underset{H_0}{\overset{H_k}{\geq}} \eta_{0,k(AMF)} \quad k = 1 \dots M \tag{28}$$

$$\Lambda_{0,k(ABORT)} = \frac{1 + \frac{\left| \frac{\hat{\Delta}^H}{S_k} \hat{R}'^{-1} \hat{\Delta} \right|^2}{\frac{\hat{\Delta}^H}{S_k} \hat{R}'^{-1} \hat{\Delta}}}{1 + \frac{\hat{\Delta}^H}{Z} \hat{R}'^{-1} \hat{\Delta} - \frac{\left| \frac{\hat{\Delta}^H}{S_k} \hat{R}'^{-1} \hat{\Delta} \right|^2}{\frac{\hat{\Delta}^H}{S_k} \hat{R}'^{-1} \hat{\Delta}}} \underset{H_0}{\overset{H_1}{\geq}} \eta_{0,k(ABORT)} \quad k = 1 \dots M \tag{29}$$

In Equation (28), $\Lambda_{0,k(AMF)}$, $k = 1 \dots M$ are computed according to Equation (19). For ease of expression, $\Lambda'_{AMF}, \eta'_{AMF}$ are replaced with $\Lambda_{0,k(AMF)}, \eta_{0,k(AMF)}$. We defined the detection results as $DT_{0,k(\bullet)}$, $k = 1 \dots M$. For detection results H_k , $DT_{0,k(\bullet)} = 1$. For detection results H_0 , $DT_{0,k(\bullet)} = 0$. According to Equations (19) and (20), for H_j against $H_{j'}$,

$$\Lambda_{k,k'(AMF)} = \frac{\left| \frac{\hat{\Delta}^H}{S_{k'}} \hat{R}'^{-1} \hat{\Delta} \right|^2}{\frac{\hat{\Delta}^H}{S_{k'}} \hat{R}'^{-1} \hat{\Delta}} \underset{H_k}{\overset{H_{k'}}{\geq}} 1 \Leftrightarrow \Lambda_{k,k'(AMF)} = \frac{\left| \frac{\hat{\Delta}^H}{S_{k'}} \hat{R}'^{-1} \hat{\Delta} \right|^2}{\frac{\hat{\Delta}^H}{S_{k'}} \hat{R}'^{-1} \hat{\Delta}} - \frac{\left| \frac{\hat{\Delta}^H}{S_k} \hat{R}'^{-1} \hat{\Delta} \right|^2}{\frac{\hat{\Delta}^H}{S_k} \hat{R}'^{-1} \hat{\Delta}} = \Lambda_{0,k'(AMF)} - \Lambda_{0,k(AMF)} \underset{H_k}{\overset{H_{k'}}{\geq}} 0 \quad \begin{matrix} k, k' = 1 \dots M, \\ k \neq k' \end{matrix} \tag{30}$$

$$\Lambda_{k,k'(ABORT)} = \Lambda_{0,k'(ABORT)} - \Lambda_{0,k(ABORT)} \underset{H_k}{\overset{H_{k'}}{\geq}} 0$$

$$\Leftrightarrow \frac{1 + \frac{\left| \frac{\hat{\Delta}^H}{S_{k'}} \hat{R}'^{-1} \hat{\Delta} \right|^2}{\frac{\hat{\Delta}^H}{S_{k'}} \hat{R}'^{-1} \hat{\Delta}}}{1 + \frac{\hat{\Delta}^H}{Z} \hat{R}'^{-1} \hat{\Delta} - \frac{\left| \frac{\hat{\Delta}^H}{S_{k'}} \hat{R}'^{-1} \hat{\Delta} \right|^2}{\frac{\hat{\Delta}^H}{S_{k'}} \hat{R}'^{-1} \hat{\Delta}}} - \frac{1 + \frac{\left| \frac{\hat{\Delta}^H}{S_k} \hat{R}'^{-1} \hat{\Delta} \right|^2}{\frac{\hat{\Delta}^H}{S_k} \hat{R}'^{-1} \hat{\Delta}}}{1 + \frac{\hat{\Delta}^H}{Z} \hat{R}'^{-1} \hat{\Delta} - \frac{\left| \frac{\hat{\Delta}^H}{S_k} \hat{R}'^{-1} \hat{\Delta} \right|^2}{\frac{\hat{\Delta}^H}{S_k} \hat{R}'^{-1} \hat{\Delta}}} \underset{H_k}{\overset{H_{k'}}{\geq}} 0 \quad \begin{matrix} k, k' = 1 \dots M, \\ k \neq k' \end{matrix} \tag{31}$$

where the symbol " \Leftrightarrow " means that the two equations are equivalent.

As shown in Figure 3, the scheme includes the detection of the moving targets, assignment, and relocation of the detected targets to the true road positions. In Figure 3, for the first detection step, the steering vector estimation results are directly integrated into the MHT technique with Equation (28) or (29), which are derived from the interferometric phase map. After the first detection step, when $\max(DT_{0,1(\bullet)}, DT_{0,2(\bullet)}, \dots, DT_{0,M(\bullet)}) < 0$ for no target is declared, the detection strategy goes to the next image pixel. When $\max(DT_{0,1(\bullet)}, DT_{0,2(\bullet)}, \dots, DT_{0,M(\bullet)}) > 0$ for one or more targets is declared, the second step is classification to decide the true corresponding road that the detected targets belong to with Equation (30) or (31). For the third step, the detected targets are relocated to their real positions, based on the detection and classification results.

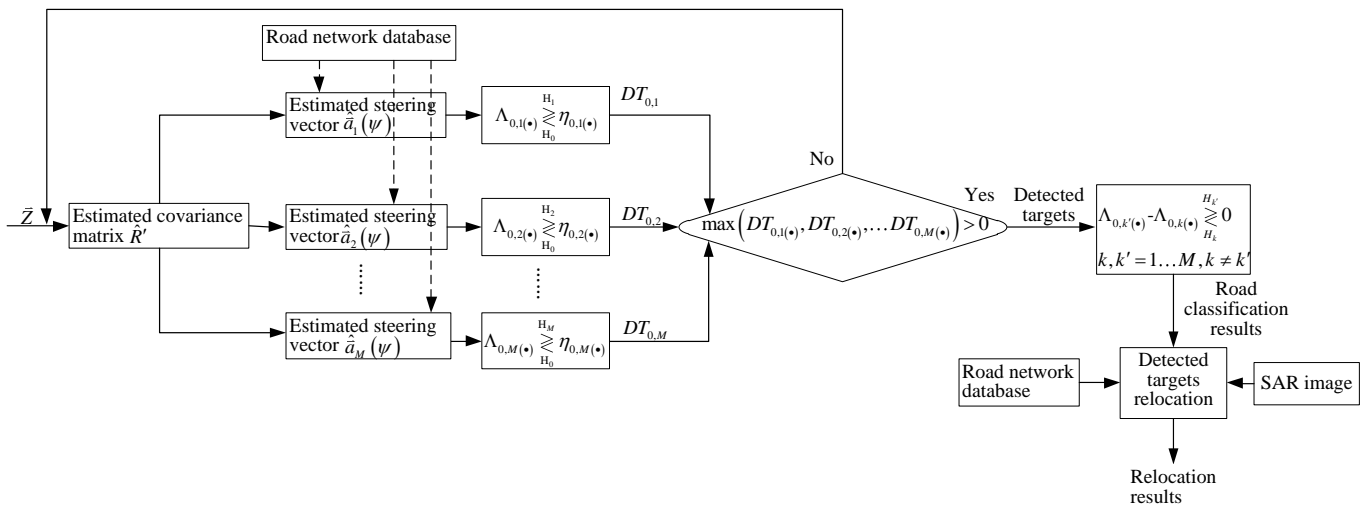


Figure 3. Detection, classification, and relocation scheme of multiple hypothesis testing technique.

To evaluate the performance of the proposed scheme, we calculate the P_{fa} , the P_d , and the probability of correct classification (P_c). The P_{fa} is defined as the probability to decide one of the M hypotheses when H_0 is true. The “total” P_{fa} can be expressed using the inclusion–exclusion principle [35,36],

$$\begin{aligned}
 P_{fa} &= P\left\{ \left(\Lambda_{0,1}(\bullet) > \eta_{0,1}(\bullet) | H_0 \right) \cup \left(\Lambda_{0,2}(\bullet) > \eta_{0,2}(\bullet) | H_0 \right) \dots \dots \cup \left(\Lambda_{0,M}(\bullet) > \eta_{0,M}(\bullet) | H_0 \right) \right\} \\
 &= \sum_{i=1}^M P\left(\Lambda_{0,i}(\bullet) > \eta_{0,i}(\bullet) | H_0 \right) - \sum_{1 \leq i < j \leq M} P\left(\Lambda_{0,i}(\bullet) > \eta_{0,i}(\bullet), \Lambda_{0,j}(\bullet) > \eta_{0,j}(\bullet) | H_0 \right) \\
 &\quad + \sum_{1 \leq i < j < k \leq M} P\left(\Lambda_{0,i}(\bullet) > \eta_{0,i}(\bullet), \Lambda_{0,j}(\bullet) > \eta_{0,j}(\bullet), \Lambda_{0,k}(\bullet) > \eta_{0,k}(\bullet) | H_0 \right) - \dots \dots \\
 &\quad + (-1)^{M-1} P\left(\Lambda_{0,1}(\bullet) > \eta_{0,1}(\bullet), \dots, \Lambda_{0,M}(\bullet) > \eta_{0,M}(\bullet) | H_0 \right)
 \end{aligned}
 \tag{32}$$

In Equation (32), the LRT functions $\Lambda_{0,1}(\bullet), \dots, \Lambda_{0,k}(\bullet), k = 2, \dots, M$ may be not mutually independent, which makes it very difficult to calculate the joint pdf of $\Lambda_{0,1}(\bullet), \dots, \Lambda_{0,k}(\bullet), k = 2, \dots, M$ under hypothesis H_0 and the “total” P_{fa} . Based on the Figure 3, the “total” P_{fa} needs to be assigned to the M independent detectors $\Lambda_{0,k}(\bullet), k = 1 \dots M$. $P\left(\Lambda_{0,k}(\bullet) > \eta_{0,k}(\bullet) | H_0 \right), k = 1, \dots, M$ can be called “local” probabilities of false alarm. In the spaceborne SAR-GMTI applications, we always need the “total” $P_{fa} \leq 10^{-5}$. Therefore, the joint terms, such as $P\left(\Lambda_{0,i}(\bullet) > \eta_{0,i}(\bullet), \Lambda_{0,j}(\bullet) > \eta_{0,j}(\bullet) | H_0 \right), 1 \leq i < j \leq M$, in the second part of Equation (32), are much less than the first “local” probabilities of false alarm items, which is generally negligible.

To compute the “total” P_{fa} , we would use the approximation as follows,

$$P_{fa} \approx \sum_{i=1}^M P\left(\Lambda_{0,i}(\bullet) > \eta_{0,i}(\bullet) | H_0 \right)
 \tag{33}$$

We assume that the “local” P_{fa} pertaining to the different roads are all the same. For given probabilities of false alarm, such as $P_{fa} \leq 10^{-5}$, the “total” P_{fa} can be divided equally to the “local” P_{fa} . The threshold $\eta_{0,k}(\bullet), k = 1, \dots, M$ are selected in order to provide the desired “total” and “local” P_{fa} . The thresholds $\eta_{0,k}(\bullet), k = 1, \dots, M$ and “local” P_{fa} can be determined by the Equations (18)–(26). Since the “local” P_{fa} is assumed the same, the thresholds $\eta_{0,1}(\bullet) = \eta_{0,2}(\bullet) = \dots = \eta_{0,M}(\bullet)$, according to Equations (18)–(26).

The P_d is defined as the probability to decide any one of the M hypotheses, when any one of these M hypotheses is true. The P_d can be expressed as [33,35,36],

$$\begin{aligned}
 P_d &= \frac{P\{(\Lambda_{0,1(\bullet)} > \eta_{0,1(\bullet)} | H_1) \cup \dots \cup (\Lambda_{0,M(\bullet)} > \eta_{0,M(\bullet)} | H_1)\} P(H_1) + \dots + P\{(\Lambda_{0,1(\bullet)} > \eta_{0,1(\bullet)} | H_M) \cup \dots \cup (\Lambda_{0,M(\bullet)} > \eta_{0,M(\bullet)} | H_M)\} P(H_M)}{P(H_1 \cup H_2 \cup \dots \cup H_M)} \\
 &= \frac{P\{(\Lambda_{0,1(\bullet)} > \eta_{0,1(\bullet)} | H_1) \cup \dots \cup (\Lambda_{0,M(\bullet)} > \eta_{0,M(\bullet)} | H_1) | H_1\} P(H_1) + \dots + P\{(\Lambda_{0,1(\bullet)} > \eta_{0,1(\bullet)} | H_M) \cup \dots \cup (\Lambda_{0,M(\bullet)} > \eta_{0,M(\bullet)} | H_M)\} P(H_M)}{P(H_1) + P(H_2) + \dots + P(H_M)} \quad (34) \\
 &= \frac{P_{d|H_1} P(H_1) + P_{d|H_2} P(H_2) + \dots + P_{d|H_M} P(H_M)}{P(H_1) + P(H_2) + \dots + P(H_M)}
 \end{aligned}$$

Under the assumption $P(H_1) = P(H_2) = \dots = P(H_M)$, Equation (34) can be expressed as,

$$P_d = \frac{1}{M} \sum_{l=1}^M P_{d|H_l} \quad (35)$$

$$\begin{aligned}
 P_{d|H_l} &= P\{(\Lambda_{0,1(\bullet)} > \eta_{0,1(\bullet)} | H_l) \cup (\Lambda_{0,2(\bullet)} > \eta_{0,2(\bullet)} | H_l) \dots \cup (\Lambda_{0,M(\bullet)} > \eta_{0,M(\bullet)} | H_l)\} \\
 &= \sum_{i=1}^M P(\Lambda_{0,i(\bullet)} > \eta_{0,i(\bullet)} | H_l) - \sum_{1 \leq i < j \leq M} P(\Lambda_{0,i(\bullet)} > \eta_{0,i(\bullet)}, \Lambda_{0,j(\bullet)} > \eta_{0,j(\bullet)} | H_l) \\
 &\quad + \sum_{1 \leq i < j < k \leq M} P(\Lambda_{0,i(\bullet)} > \eta_{0,i(\bullet)}, \Lambda_{0,j(\bullet)} > \eta_{0,j(\bullet)}, \Lambda_{0,k(\bullet)} > \eta_{0,k(\bullet)} | H_l) - \dots \\
 &\quad + (-1)^{M-1} P(\Lambda_{0,1(\bullet)} > \eta_{0,1(\bullet)}, \dots, \Lambda_{0,M(\bullet)} > \eta_{0,M(\bullet)} | H_l) \quad , l = 1, \dots, M \quad (36)
 \end{aligned}$$

We can use the notation as follows [35,37],

$$PL_1 = \sum_{i=1}^M P(\Lambda_{0,i(\bullet)} > \eta_{0,i(\bullet)} | H_l) \quad (37)$$

$$PL_k = \sum_{1 \leq i_1 < \dots < i_k \leq M} P(\Lambda_{0,i_1(\bullet)} > \eta_{0,i_1(\bullet)}, \dots, \Lambda_{0,i_k(\bullet)} > \eta_{0,i_k(\bullet)} | H_l), \quad k = 2, \dots, M \quad (38)$$

Then the “local” P_d can be expressed as,

$$P_{d|H_l} = \sum_{i=1}^M (-1)^{i-1} PL_i \quad (39)$$

To simplify the computation of Equations (36) and (39), we can use the expression as follows [38,39],

$$\begin{aligned}
 P_{d|H_l} &= P\{(\Lambda_{0,1(\bullet)} > \eta_{0,1(\bullet)} | H_l) \cup (\Lambda_{0,2(\bullet)} > \eta_{0,2(\bullet)} | H_l) \dots \cup (\Lambda_{0,M(\bullet)} > \eta_{0,M(\bullet)} | H_l)\} \\
 &= 1 - P(\Lambda_{0,1(\bullet)} < \eta_{0,1(\bullet)}, \dots, \Lambda_{0,M(\bullet)} < \eta_{0,M(\bullet)} | H_l) \quad (40)
 \end{aligned}$$

$\Lambda_{0,1(\bullet)}, \Lambda_{0,2(\bullet)}, \dots, \Lambda_{0,M(\bullet)}$ may not be mutually independent, which makes it very difficult to calculate the joint probability density function and the probability in Equation (40). Performance is investigated by means of numerical analysis and Monte Carlo simulation in terms of P_d . Firstly, we set $P_{fa} = 10^{-5}$ and assume that the “local” P_{fa} pertaining to the different roads are all the same. For given probabilities of false alarm, the “total” P_{fa} can be divided equally to the “local” P_{fa} . We calculated the “local” thresholds $\eta_{0,1(\bullet)}, \eta_{0,2(\bullet)}, \dots, \eta_{0,M(\bullet)}$ by using Equations (18)–(26) and (33). Then, we employed the Monte Carlo technique to approximate the integration in Equation (40) and calculate “total” and “local” P_d by running 100,000 Monte Carlo runs.

The probability of correct classification P_c is defined as the probability of deciding for the correct hypothesis when a target is present and belongs to one of the M roads, that is,

$$\begin{aligned}
 P_c &= \frac{P(\hat{H}_1|H_1)P(H_1) + P(\hat{H}_2|H_2)P(H_2) \dots + P(\hat{H}_M|H_M)P(H_M)}{P(H_1) + P(H_2) \dots + P(H_M)} \\
 &= \frac{P_{c|H_1} P(H_1) + P_{c|H_2} P(H_2) + \dots + P_{c|H_M} P(H_M)}{P(H_1) + P(H_2) + \dots + P(H_M)} \quad (41)
 \end{aligned}$$

Under the assumption $P(H_1) = P(H_2) = \dots = P(H_M)$, Equation (41) can be expressed as,

$$P_c = \frac{1}{M} \sum_{l=1}^M P_{c|H_l} \tag{42}$$

As shown in the front part, for given probabilities of false alarm, the “total” P_{fa} can be divided equally to the “local” P_{fa} . The thresholds $\eta_{0,1(\bullet)} = \eta_{0,2(\bullet)} = \dots = \eta_{0,M(\bullet)}$. So $P_{c|H_l}$ can be expressed using the inclusion–exclusion principle [35,36],

$$P_{c|H_l} = P \left\{ \left(\Lambda_{0,l(\bullet)} > \eta_{0,l(\bullet)} | H_l \right), \bigcap_{i=1, i \neq l}^M \left(\Lambda_{i,l(\bullet)} > 1 | H_l \right) \right\} \tag{43}$$

or $P_{c|H_l} = P \left(\Lambda_{0,l(\bullet)} > \eta_{0,l(\bullet)}, \Lambda_{i,l(\bullet)} > 1, \dots, \Lambda_{M,l(\bullet)} > 1 | H_l \right) i = 1, \dots, M, l = 1, \dots, M, i \neq l$

As shown in the front part, it is very difficult to calculate the joint probability density function and the probability in the Equations (42) and (43). For performance analysis, we resorted to numerical integration to calculate them, which is a show of good performance under the Monte Carlo simulation.

Figure 4 shows plots of the Pd and Pc versus input SCNR ($SCNR_{in}$) of the proposed MHT technique based on the AMF and the ABORT with parameters $L = 49$, $K = 6$, $M = 4$, and $P_{fa} = 10^{-5}$. The “total” probabilities of false alarm are divided equally to the “local” Pfa. The Monte Carlo runs are 100,000. Moving targets are modeled as point targets of the Swerling 0 case. In Figure 4a, Pd versus $SCNR_{in}$ of the two detection techniques for $\psi_{H_1} = 1.0rad$, $\psi_{H_2} = 1.5rad$, $\psi_{H_3} = 1.1rad, -1.2rad$, $\psi_{H_4} = -1.5rad$ are shown. In Figure 4b, Pc versus $SCNR_{in}$ for $\psi_{H_1} = 1.0rad$, $\psi_{H_2} = 1.5rad$, $\psi_{H_3} = 1.1rad, -1.2rad$, $\psi_{H_4} = -1.5rad$ is shown. In Figure 4c, Pd versus $SCNR_{in}$ for $\psi_{H_1} = 1.0rad$, $\psi_{H_2} = 1.5rad$, $\psi_{H_3} = 1.1rad, -1.2rad$, $\psi_{H_4} = 0.9rad$ is shown. In Figure 4d, Pc versus $SCNR_{in}$ for $\psi_{H_1} = 1.0rad$, $\psi_{H_2} = 1.5rad$, $\psi_{H_3} = 1.1rad, -1.2rad$, $\psi_{H_4} = 0.9rad$ is shown. The figures show that Pd and Pc increase with $SCNR_{in}$ and it is easier to detect the presence of a target rather than classify them to the corresponding road. Pd and Pc increase with the phase difference for different corresponding roads and it is easier to detect and classify the targets for larger phase differences. The figures also show that AMF has a similar detection and classification performance to ABORT. From computational considerations, it is less costly to compute the AMF statistic since it does not require the computation of the term $Z^H \hat{R}^{-1} Z$. Therefore, we may use the AMF statistic to the proposed multiple hypothesis testing technique. In Figure 4, the probability of correct classification increases with the enlargement of the interferometric phase difference. It is more difficult to classify the detected targets to the corresponding roads when the interferometric phase or steering vectors are very close to each other.

For the ordinary SAR-GMTI techniques [2–5,11–14], the search results of the steering vectors and the interferometric phase estimation are always exploited to estimate the Δa and relocate the detected targets, which may include ambiguities and estimation errors. In this paper, based on the priori knowledge of the road network, Δa can be directly applied to relocate the detected targets. Based on the proposed detection, classification, and relocation scheme, as shown in Figure 3, the detected targets can be classified and relocated to the corresponding road segments. There may be some kinds of errors which influence the estimation accuracy of the target’s true position within the stationary SAR images. For example, the road axis position errors determined by the accuracy of road network database may propagate to the azimuth displacement estimation. The azimuth resolution and sample interval can influence the relocation accuracy. These errors have been analyzed and presented in many SAR-GMTI techniques [2–5,11–14]. In the proposed technique, the detected targets may be classified to the wrong road segments because the probability of correct classification P_c is very small under low-input SCNR or the steering vectors corresponding to different roads are very close as shown in Figure 4. The classification error is the major error which influences the relocation accuracy in the proposed technique.

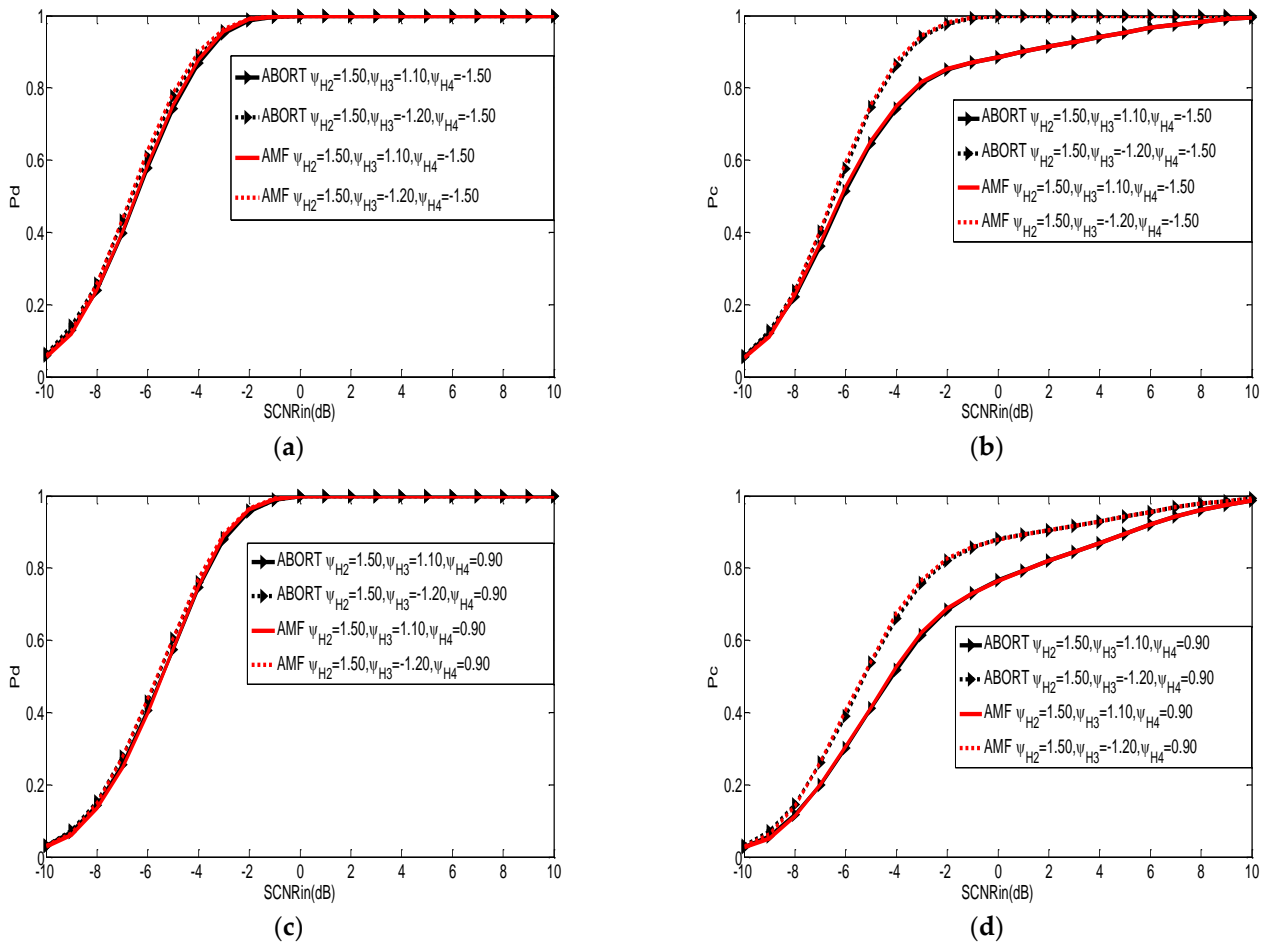


Figure 4. Pd and Pc versus $SCNR_{in}$ of the proposed multiple hypothesis testing technique based on ABORT and AMF. (a) $\psi_{H_1} = 1.0$ rad, $\psi_{H_2} = 1.5$ rad, $\psi_{H_3} = 1.1$ rad, $\psi_{H_4} = -1.5$ rad; (b) $\psi_{H_1} = 1.0$ rad, $\psi_{H_2} = 1.5$ rad, $\psi_{H_3} = 1.1$ rad, $\psi_{H_4} = -1.5$ rad; (c) $\psi_{H_1} = 1.0$ rad, $\psi_{H_2} = 1.5$ rad, $\psi_{H_3} = 1.1$ rad, $\psi_{H_4} = 0.9$ rad; (d) $\psi_{H_1} = 1.0$ rad, $\psi_{H_2} = 1.5$ rad, $\psi_{H_3} = 1.1$ rad, $\psi_{H_4} = 0.9$ rad.

5. Simulation Experimental Results

Compared with a two-channel or multichannel spaceborne SAR system, such as the Italian COSMO-SkyMed [40], the German TerraSAR-X [11–14], and the Canadian Radarsat-2 [27], the distributed SAR systems provide the possibility to detect slowly moving targets based on large along-track baselines and enhance the moving target velocity estimation accuracy based on multiple baselines. Satellite formation, radar system and raw data simulation, and SAR-GMTI signal processing are the crucial problems to verify distributed spaceborne SAR system design and analyze signal processing technique performance. The SBRAS is an economical software developed by our lab [15,22–25], and the capabilities include satellites simulation, radar system simulation, SAR raw data simulation, monostatic/bistatic/multistatic SAR imaging, InSAR (interferometric synthetic aperture radar) processing, Digital Elevation Model (DEM) generation, GMTI/SAR-GMTI signal processing, system and signal processing performance analysis, and many other functions. The main SAR-GMTI simulation flow chart based on SBRAS is shown in Figure 5. To verify the above clutter suppression and moving target detection algorithm, some simulation experiments and analyses are developed on SBRAS [15,22–25]. The multistatic SAR images, which include moving targets, are simulated based on SBRAS. We use the proposed method to the clutter cancellation, moving target detection, target relocation, and performance analysis.

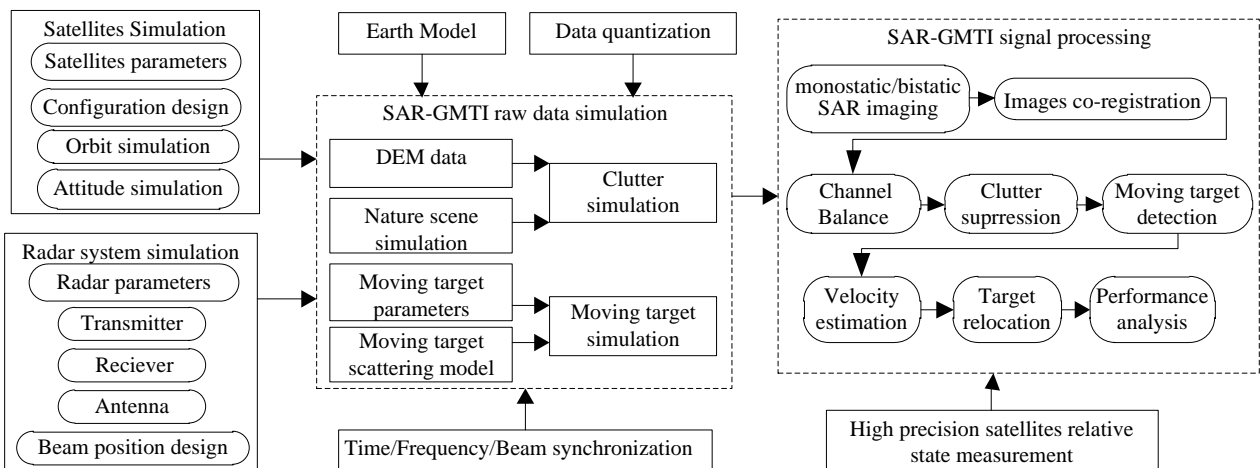


Figure 5. Distributed spaceborne SAR-GMTI simulation flow chart.

The simulated SAR image, the interferometric phase map derived from the road database, and azimuth displacement map are presented in Figure 6. The simulation parameters are: satellite speed $v_s = 7.5$ Km/s, altitude $H = 514$ Km, the number of satellites $K = 6$, antenna size (length \times width) $7\text{ m} \times 0.5\text{ m}$, wavelength $\lambda = 0.0563\text{ m}$, $PRF = 2.9\text{ KHz}$, chirp bandwidth $BW = 50\text{ MHz}$, incidence angle $\theta_{inc} = 30^\circ$, and pulse width $PW = 35\ \mu\text{s}$. The satellites fly on the SAR-Train formation with uniform along-track baseline $B = 150\text{ m}$.

The master satellite does both transmit and receive, while other slave satellites only receive the radar echo. The simulated static scene is composed of several fields with different kinds of mean RCS, which include trees, buildings, roads, and so on. Additionally, there are eighteen simulated targets driving along the road, which are modeled as point targets. Figure 6a shows the simulated master satellite SAR image. In Figure 6a, the moving targets are buried within the clutter, which cannot be directly detected. Figure 6b shows the road map, which is derived from the road network database and the master satellite SAR image. In Figure 6c, the interferometric phase map is derived according to Equations (12)–(14), which only shown within $[-\pi, +\pi]$ to see with ease. In Figure 6d, the azimuth displacement map can also be derived from Equations (12)–(14) pixel by pixel, which also only show within small range corresponding to the interferometric phase map. For the proposed MHT technique, the entire phase map and displacement map should be applied to steering vector estimation and clutter suppression.

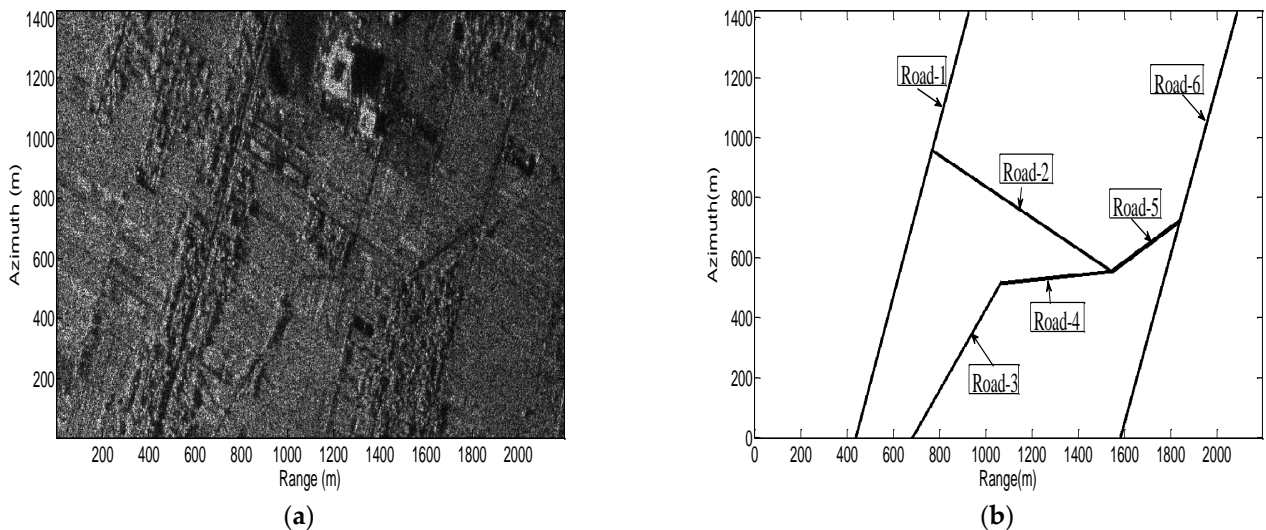


Figure 6. Cont.

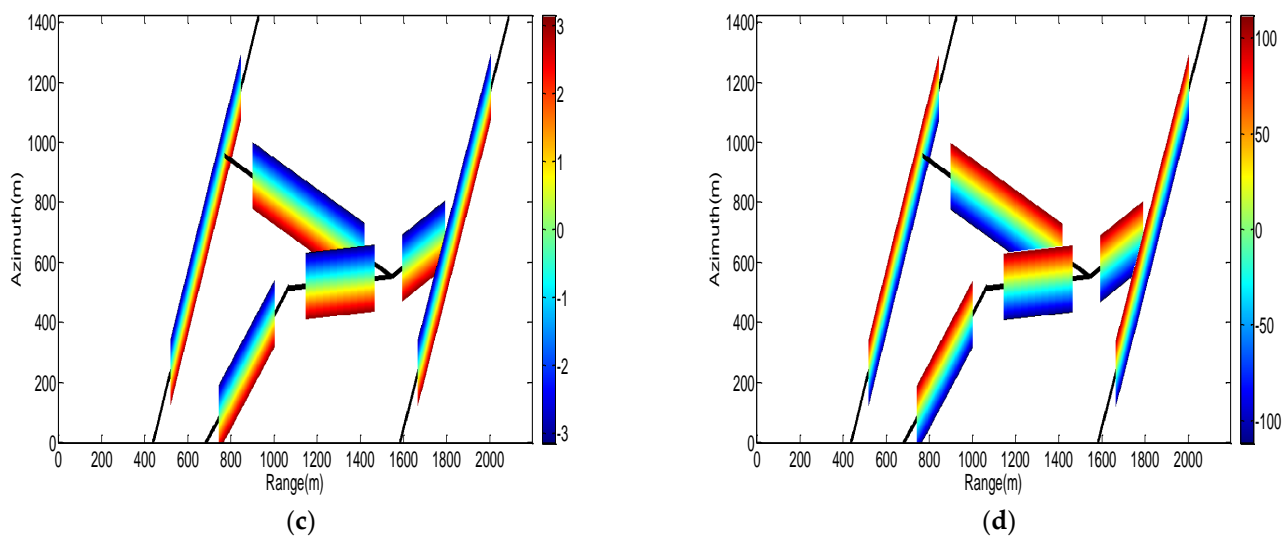


Figure 6. Master satellite SAR image, road map, interferometric phase map, and azimuth displacement map derived from road database. (a) Master satellite SAR image; (b) road map; (c) interferometric phase map; (d) azimuth displacement map derived from road database.

The SAR-GMTI signal processing simulation results are shown in Figure 7, in which the simulation static scene, satellites, and radar parameters are the same as in Figure 6. Some SAR-GMTI signal processing steps, which include monostatic/bistatic SAR imaging, coregistration, and channel balance, exploited the techniques developed on SBRAS. In the simulations of Figure 7, the proposed MHT technique uses the AMF statistic for computational considerations.

Figure 7a shows the real positions (or priori positions) as the “red dots” of the eighteen simulated moving targets. There are five targets moving on road-1 with ground radial velocities $v_r = 2, 4, -4, -8, -12$ m/s, according to the road marking in Figure 6b; six targets moving on road-2 with $v_r = 6, 9, 12, -1, -5, -10$ m/s; two targets moving on road-4 with $v_r = 1.5, 8$ m/s; one target moving on road-5 with $v_r = 4.5$ m/s; and four targets moving on road-6 with $v_r = 1, 3, 5, 13.5$ m/s. Figure 7b shows the traditional AMF technique detection results use Equations (20) and (21) with $P_{fa} = 10^{-5}$. In Figure 7b, the “red dots” represent the accurate detection results and the “green dots” represent the false alarms. In Figure 7b, it can be observed that some “green dots” for the residual clutter regions and the eighteen real moving targets have been detected completely. Figure 7c shows the detection results of the proposed method with $P_{fa} = 10^{-5}$, in which the “red dots” represent the accurate detection results and the “green dots” represent the false alarms. It can be observed that the eighteen moving targets have been detected completely with some false alarms. Figure 7d shows the relocation results of the proposed method, whose detection results are shown in Figure 7c. In Figure 7d, the “red dots” represent the accurate detection and relocation results and “green dots” represent the false alarms. The “blue dots” represent the accurate detection and false relocation results. A bit of accurately detected results and false alarms, whose relocated positions are the same, have been marked by “red dots”. It can be observed that sixteen moving targets have been correctly relocated and two targets have been relocated in the wrong roads because the probability of correct classification is low for low input SCNR cases. Based on the proposed technique, the false alarms are also relocated to the corresponding roads. Some false alarms, whose relocated positions are very close to each other or close to the false relocation dots, have been overlapped by each other or overlapped by the “blue dots”.

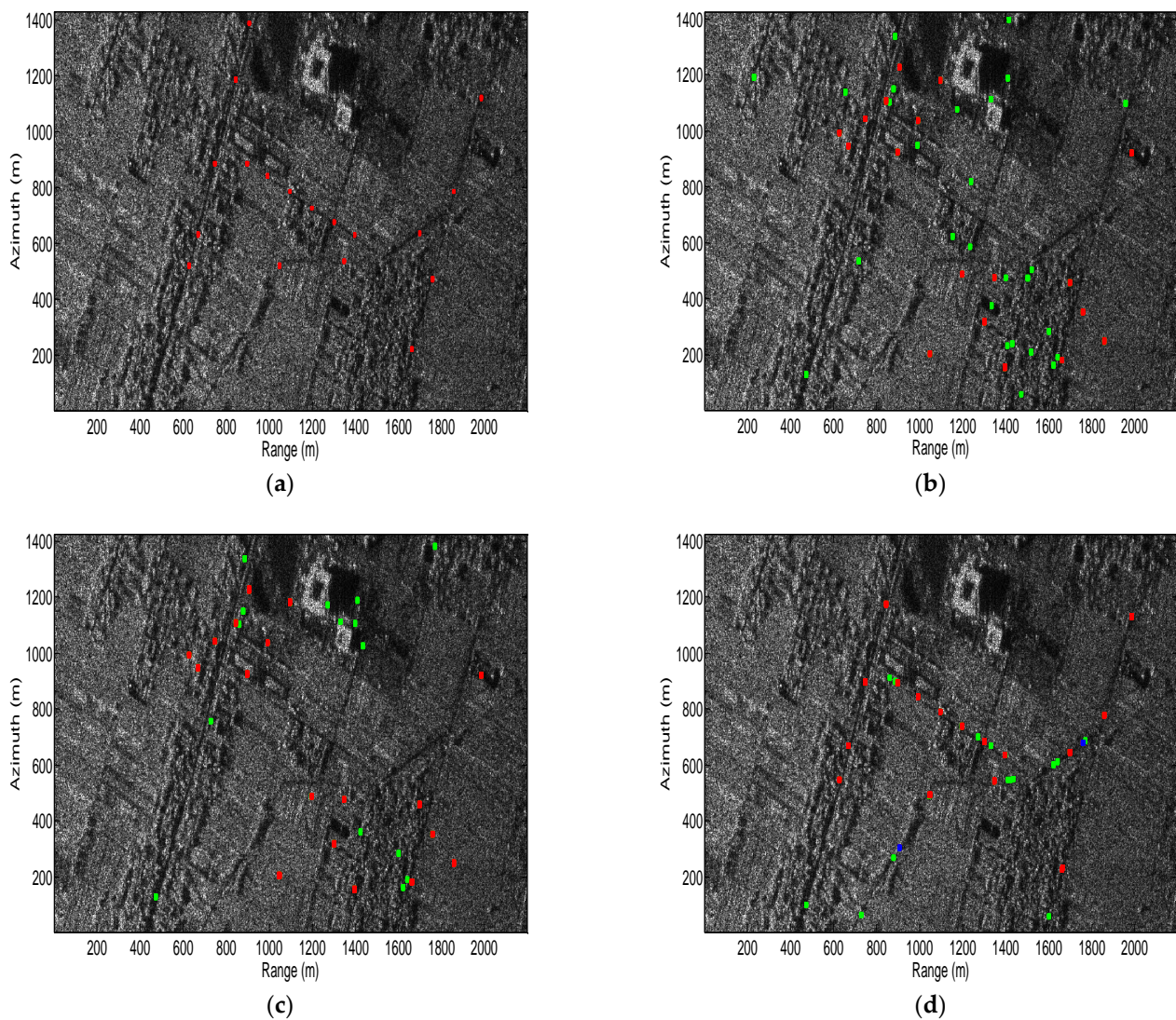


Figure 7. The SAR-GMTI signal processing results for AMF and the proposed method. (a) real positions of the eighteen simulated moving targets (red dots); (b) traditional AMF technique detection results (red dots represent the accurate detection results, green dots represent the false alarms); (c) detection results of the proposed method (red dots represent the accurate detection results, green dots represent the false alarms); (d) relocation results of the proposed method (red dots represent the accurate detection and relocation results, green dots represent the false alarms, blue dots represent the accurate detection and false relocation results).

6. Discussion

For military use, spaceborne SAR-GMTI systems can detect ground moving vehicles and estimate their parameters. For civilian use, spaceborne SAR-GMTI systems can monitor the traffic situation in urban and motorway areas. For traffic monitoring use, a ground vehicle may move strictly on the road with a maximum or minimum velocity limitation and velocity direction limitation. For SAR-GMTI processing, the ground moving vehicles may be detected and relocated to a certain road. The road network information can be exploited as a priori knowledge to improve the SAR-GMTI signal processing performance.

The proposed method has many advantages. Firstly, most of the existing SAR-GMTI processing methods assume that no prior information can be used, which is appropriate for military use. For civilian applications, especially for traffic monitoring use, the off-road moving targets can be ignored based on the a priori known road network. This

operation in the SAR-GMTI processing may reduce the signal processing complexity and computational load.

Secondly, the P_d versus $\cos^2(\theta)$ is shown in Figures 1 and 2 for AMF and ABORT. P_d and P_c versus $SCNR_{in}$ of the proposed multiple hypothesis testing technique is shown in Figure 4, which is based on ABORT and AMF. For the large mismatch angle θ , the P_d may decrease quickly and approximate to zero. Based on the priori knowledge of the road network database, the moving target steering vectors may be estimated accurately. As shown in Figure 4, even under low input SCNR, the P_d is still high enough to detect the presence of a target. The proposed technique eliminated the influence of the steering vector mismatch for the detection performance of the adaptive clutter suppression technique.

Thirdly, the integration of a priori knowledge into SAR-GMTI processing may improve the moving vehicles parameter estimation accuracy. Due to the relation of the along-track interferometric phase and the target velocity in the across-track direction, the interferometric phase is always exploited to estimate the moving target velocity parameters and relocate the moving target to its real position. However, as shown in Figure 7, the traditional AMF technique may not relocate the detected targets because the target's interferometric phase estimation may be wrapped within $[-\pi, +\pi]$ for large radial velocities. The interferometric phase may also be influenced by clutter and noise. The proposed method performs velocity estimation based on the along-track displacement of detected vehicles from their corresponding roads. The multiple hypothesis testing technique and the azimuth displacement map are exploited to resolve the potential ambiguities. The incorporated road data not only improves the estimation accuracy but also limits the search space. As shown in Figure 7, based on the priori knowledge of road network information, the proposed method may detect the moving targets effectively and relocate them to the real positions with a small number of relocation errors because of the corresponding road classification errors.

7. Conclusions

In this paper, we have proposed a priori knowledge-based adaptive clutter cancellation and moving target detection technique for SAR-GMTI applied to the distributed spaceborne SAR systems. A priori knowledge, such as the road network database, is integrated into the adaptive processor to reduce any moving target steering vector mismatch. Two kinds of adaptive detection techniques are exploited for moving target detection. The MHT technique is proposed to detect the moving targets and resolve the moving target steering vector estimation ambiguity for the dense road network cases. For the MHT technique, AMF and ABORT have similar detection and classification performance. SBRAS developed by our research group has been exploited to simulate the multistatic spaceborne SAR transmitted signals and received echoes. Based on the SBRAS, the SAR-GMTI signal processing simulation results have shown that the proposed method can efficiently detect the moving targets with a small number of relocation errors.

In fact, apart from the road mapping data, other knowledge of the external environment can also be integrated into the proposed adaptive clutter cancellation and moving target detection techniques. They may include the knowledge of clutter statistics of nonhomogeneous terrain and the characteristics of the moving targets. As a remark, although the distributed spaceborne SAR system is employed in the paper, the method can also be modified to other multistatic or multi-aperture (multi-antenna or multi-channel) SAR-GMTI systems. For example, the SAR satellite formations with nonuniform baselines and the spaceborne/airborne multi-channel SAR systems.

Author Contributions: Conceptualization, B.C.; data curation, X.H.; formal analysis, L.C. and J.L.; funding acquisition, B.C.; investigation, L.C. and J.L.; methodology, B.C.; project administration, J.L.; resources, X.H.; software, X.H.; supervision, L.C.; validation, B.C.; visualization, T.C. and Y.L.; writing—original draft, B.C.; writing—review & editing, T.C. and Y.L. All authors have read and agreed to the published version of the manuscript.

Funding: This research was funded by the National Natural Science Foundation of China under Grant 61871396.

Institutional Review Board Statement: Not applicable.

Data Availability Statement: Not applicable.

Acknowledgments: The authors would like to thank the handling editor and the anonymous reviewers for their valuable comments and suggestions for this paper.

Conflicts of Interest: The authors declare no conflict of interest.

Abbreviations

The following abbreviations are used in this manuscript:

SAR	synthetic aperture radar
GMTI	ground moving target indication
DOF	degree of freedoms
AMF	adaptive matched filter
ABORT	adaptive beamformer orthogonal rejection test
MHT	multiple hypothesis testing
MDV	minimum detectable velocity
ATI	along track interferometric
DPCA	displaced phase center antenna
TSX	TerraSAR-X
TDX	TanDEM-X
SCNR	signal-to-clutter plus noise ratio
SBRAS	SpaceBorne Radar Advanced Simulator
i.i.d.	independent and identically distributed
ML	maximum likelihood
STAP	space time adaptive processing
RCS	radar cross-section
GLRT	generalized likelihood ratio test
ACE	adaptive coherence estimator
ROC	Receiver Operating Characteristic
Pd	probability of detection
Pfa	probability of false alarm
LRT	likelihood ratios test
Pc	probability of correct classification
InSAR	interferometric synthetic aperture radar
DEM	digital elevation model

References

1. Paul Aguttes, J. The SAR Train Concept: An Along-Track Formation of Sar Satellites for Diluting the Antenna Area over N Smaller Satellites, While Increasing Performance by N. *Acta Astronaut.* **2005**, *57*, 197–204. [[CrossRef](#)]
2. Budillon, A.; Schirinzi, G. Performance Evaluation of a GLRT Moving Target Detector for TerraSAR-X Along-Track Interferometric Data. *IEEE Trans. Geosci. Remote Sens.* **2015**, *53*, 3350–3360. [[CrossRef](#)]
3. Suwa, K.; Yamamoto, K.; Tsuchida, M.; Nakamura, S.; Wakayama, T.; Hara, T. Image-Based Target Detection and Radial Velocity Estimation Methods for Multichannel SAR-GMTI. *IEEE Trans. Geosci. Remote Sens.* **2017**, *55*, 1325–1338. [[CrossRef](#)]
4. Sikaneta, I.C.; Gierull, C.H. Adaptive CFAR for Space-Based Multichannel SAR-GMTI. *IEEE Trans. Geosci. Remote Sens.* **2012**, *50*, 5004–5013. [[CrossRef](#)]
5. Rashid, M.; Dansereau, R.M. Cramér–Rao Lower Bound Derivation and Performance Analysis for Space-Based SAR GMTI. *IEEE Trans. Geosci. Remote Sens.* **2017**, *55*, 6031–6043. [[CrossRef](#)]
6. Krieger, G.; Moreira, A. Spaceborne Bi- and Multistatic SAR: Potential and Challenges. *IEEE Proc. Radar Sonar Navig.* **2006**, *153*, 184–198. [[CrossRef](#)]
7. Krieger, G.; Moreira, A.; Fiedler, H.; Hajnsek, I.; Werner, M.; Younis, M.; Zink, M. TanDEM-X: A Satellite Formation for High-Resolution SAR Interferometry. *IEEE Trans. Geosci. Remote Sens.* **2007**, *45*, 3317–3341. [[CrossRef](#)]
8. Li, Z.F.; Bao, Z.; Yang, F.F. Ground Moving Target Detection and Location Based on SAR Images for Distributed Spaceborne SAR. *Sci. China Ser. F* **2005**, *48*, 632–646. [[CrossRef](#)]

9. Yang, Z.W.; Liao, G.S.; Zeng, C. Reduced-Dimensional Processing for Ground Moving Target Detection in Distributed Space-Based Radar. *IEEE Geosci. Remote Sens. Lett.* **2007**, *4*, 256–259. [[CrossRef](#)]
10. He, X.P.; Liao, G.S.; Xu, J.W.; Zhu, S.Q. Robust Radial Velocity Estimation Based on Joint-Pixel Normalized Sample Covariance Matrix and Shift Vector for Moving Targets. *IEEE Geosci. Remote Sens. Lett.* **2019**, *16*, 221–225. [[CrossRef](#)]
11. Meyer, F.; Hinz, S.; Laika, A.; Wehling, D.; Bamler, R. Performance Analysis of the TerraSAR-X Traffic Monitoring Concept. *ISPRS J. Photogramm. Remote Sens.* **2006**, *61*, 225–242. [[CrossRef](#)]
12. Hinz, S.; Meyer, F.; Laika, A.; Bamler, R. Spaceborne Traffic Monitoring with Dual Channel Synthetic Aperture Radar Theory and Experiments. In Proceedings of the 2005 IEEE Computer Society Conference on Computer Vision and Pattern Recognition (CVPR'05)—Workshops, San Diego, CA, USA, 21–23 September 2005; pp. 89–94. [[CrossRef](#)]
13. Meyer, F.; Hinz, S.; Laika, A.; Bamler, R. A-Priori Information Driven Detection of Moving Objects for Traffic Monitoring by SAR. In Proceedings of the 2005 IEEE International Geoscience and Remote Sensing Symposium, Seoul, Republic of Korea, 25–29 July 2005; Volume 4, pp. 2932–2936. [[CrossRef](#)]
14. Meyer, F.; Hinz, S. The Feasibility of Traffic Monitoring with TerraSAR-X—Analyses and Consequences. In Proceedings of the IEEE International Geoscience and Remote Sensing Symposium, Anchorage, AK, USA, 20–24 September 2004; IGARSS'04. IEEE: Anchorage, AK, USA, 2004; Volume 2, pp. 1502–1505. [[CrossRef](#)]
15. Cai, B.; Dong, Z.; Zhang, Y.; Chen, Q. Integrating a Prior Information to Spaceborne Dual-Channel SAR-GMTI. In Proceedings of the IET Conference Publications, Guilin, China, 20–22 April 2009; pp. 444–448. [[CrossRef](#)]
16. Baumgartner, S.V.; Krieger, G. Fast GMTI Algorithm For Traffic Monitoring Based On A Priori Knowledge. *IEEE Trans. Geosci. Remote Sens.* **2012**, *50*, 4626–4641. [[CrossRef](#)]
17. Baumgartner, S.V.; Krieger, G. A priori knowledge based GMTI algorithm for traffic monitoring applications. In Proceedings of the 8th European Conference on Synthetic Aperture Radar, Aachen, Germany, 7–10 June 2010; pp. 469–472.
18. Baumgartner, S.V.; Krieger, G. Real-Time Road Traffic Monitoring Using a Fast a Priori Knowledge Based SAR-GMTI Algorithm. In Proceedings of the 2010 IEEE International Geoscience and Remote Sensing Symposium, Honolulu, HI, USA, 25–30 July 2010; pp. 1843–1846. [[CrossRef](#)]
19. Huang, P.; Zhang, X.; Zou, Z.; Liu, X.; Liao, G.; Fan, H. Road-Aided Along-Track Baseline Estimation in a Multichannel SAR-GMTI System. *IEEE Geosci. Remote Sens. Lett.* **2021**, *18*, 1416–1420. [[CrossRef](#)]
20. Budillon, A.; Gierull, C.H.; Pascasio, V.; Schirinzi, G. Along-Track Interferometric SAR Systems for Ground-Moving Target Indication: Achievements, Potentials, and Outlook. *IEEE Geosci. Remote Sens. Mag.* **2020**, *8*, 46–63. [[CrossRef](#)]
21. Song, C.; Wang, B.; Xiang, M.; Li, W. Extended GLRT Detection of Moving Targets for Multichannel SAR Based on Generalized Steering Vector. *Sensors* **2021**, *21*, 1478. [[CrossRef](#)]
22. Pan, W.; Cai, B. Robust Adaptive Ground Moving Target Indication Technique Applied to Distributed Spaceborne SAR System. In Proceedings of the 2010 International Conference on Computer Application and System Modeling (ICCSM 2010), Taiyuan, China, 22–24 October 2010; pp. V5-289–V5-293. [[CrossRef](#)]
23. Cai, B. Research on Signal Processing of Distributed Spaceborne InSAR and SAR-GMTI. Ph.D. Thesis, National University of Defense Technology, Changsha, China, 2009. [[CrossRef](#)]
24. Wang, M.; Huang, H.; Dong, Z. SBRAS—An Advanced Simulator of Spaceborne Radar. In Proceedings of the 2007 IEEE International Geoscience and Remote Sensing Symposium, Barcelona, Spain, 23–28 July 2007; pp. 4942–4944. [[CrossRef](#)]
25. He, Z.H.; He, F.; Dong, Z.; Liang, D.N. Real-Time Raw-Signal Simulation Algorithm for InSAR Hardware-in-the-Loop Simulation Applications. *IEEE Geosci. Remote Sens. Lett.* **2012**, *9*, 134–138. [[CrossRef](#)]
26. Gierull, C.H. *Digital Channel Balancing of Along-Track Interferometric SAR Data*; Technical Memorandum TM 2003-024; Defence Research Establishment Ottawa (DREO): Ottawa, ON, Canada, 2003.
27. Chiu, S.; Livingstone, C. A Comparison of Displaced Phase Centre Antenna and Along-Track Interferometry Techniques for RADARSAT-2 Ground Moving Target Indication. *Can. J. Remote Sens.* **2005**, *31*, 37–51. [[CrossRef](#)]
28. McDonald, K.F.; Blum, R.S. Exact Performance of STAP Algorithms with Mismatched Steering and Clutter Statistics. *IEEE Trans. Signal Process.* **2000**, *48*, 2750–2763. [[CrossRef](#)]
29. Pulsone, N.B.; Rader, C.M. Adaptive Beamformer Orthogonal Rejection Test. *IEEE Trans. Signal Process.* **2001**, *49*, 521–529. [[CrossRef](#)]
30. Richmond, C.D. Performance of the Adaptive Sidelobe Blanker Detection Algorithm in Homogeneous Environments. *IEEE Trans. Signal Process.* **2000**, *48*, 1235–1247. [[CrossRef](#)]
31. Robey, F.C.; Fuhrmann, D.R.; Kelly, E.J.; Nitzberg, R.A. A CFAR adaptive matched filter detector. *IEEE Trans. Aerosp. Electron. Syst.* **1992**, *28*, 208–216. [[CrossRef](#)]
32. Kelly, E.J. An adaptive detection algorithm. *IEEE Trans. Aerosp. Electron. Syst.* **1986**, *AES-22*, 115–127. [[CrossRef](#)]
33. Gini, F.; Farina, A.; Greco, M.S. Radar Detection and Preclassification Based on Multiple Hypothesis Testing. *IEEE Trans. Aerosp. Electron. Syst.* **2004**, *40*, 1046–1059. [[CrossRef](#)]
34. Green, M.; Zoubir, A.M. Multiple hypothesis testing for time-varying nonlinear system identification. In Proceedings of the 2000 IEEE International Conference on Acoustics, Speech, and Signal Processing, Istanbul, Turkey, 5–9 June 2000; Volume 1, pp. 560–563. [[CrossRef](#)]
35. Fomin, F.V.; Kratsch, D. Exact Exponential Algorithms; Texts in Theoretical Computer Science. In *An EATCS Series*; Springer: Berlin/Heidelberg, Germany, 2010; pp. 49–72. ISBN 978-3-642-16532-0.

36. Lodhi, M.A.; Bajwa, W.U. Detection Theory for Union of Subspaces. *IEEE Trans. Signal Process.* **2018**, *66*, 6347–6362. [[CrossRef](#)]
37. Grzegorzewski, P. The Inclusion–Exclusion Principle for IF-Events. *Inf. Sci.* **2011**, *181*, 536–546. [[CrossRef](#)]
38. Gaffney, C.T. The Application of the Inclusion-Exclusion Principle in Learning Monotone Boolean Functions. Master’s Thesis, University of Nevada, Reno, NV, USA, 2009.
39. Roberts, F.S.; Tesman, B. Applied Combinatorics. In *A Chapman & Hall Book*, 2nd ed.; CRC Press: Boca Raton, FA, USA, 2009; ISBN 978-1-4200-9982-9.
40. Pastina, D.; Turin, F. Exploitation of the COSMO-SkyMed SAR System for GMTI Applications. *IEEE J. Sel. Top. Appl. Earth Obs. Remote Sens.* **2015**, *8*, 966–979. [[CrossRef](#)]

Disclaimer/Publisher’s Note: The statements, opinions and data contained in all publications are solely those of the individual author(s) and contributor(s) and not of MDPI and/or the editor(s). MDPI and/or the editor(s) disclaim responsibility for any injury to people or property resulting from any ideas, methods, instructions or products referred to in the content.